The W. M. Keck Observatory Laser Guide Star Adaptive Optics System: Performance Characterization

Marcos A. van Dam, Antonin H. Bouchez, David Le Mignant, Erik M. Johansson, Peter L. Wizinowich,
Randy D. Campbell, Jason C. Y. Chin, Scott K. Hartman, Robert E. Lafon, Paul J. Stomski, Jr.,
and Douglas M. Summers

W. M. Keck Observatory, 65-1120 Mamalahoa Highway, Kamuela, HI 96743; mvandam@keck.hawaii.edu

ABSTRACT. The Keck II Telescope is the first 8–10 m class telescope equipped with a laser guide star adaptive optics (LGS AO) system. Under normal seeing conditions, the LGS AO system produces K-band Strehl ratios between 30% and 40% using bright tip-tilt guide stars, and it works well with tip-tilt guide stars as faint as $m_R = 18$, with partial correction for stars up to a magnitude fainter. This paper presents the algorithms implemented in the LGS AO system, as well as experimental performance results. A detailed error budget shows excellent agreement between the measured and expected image quality for both bright and faint guide stars.

1. INTRODUCTION

Adaptive optics (AO) has found widespread use in astronomy, providing astronomers with high-resolution images. For example, the natural guide star (NGS) AO systems on both telescopes at the W. M. Keck Observatory achieve diffraction-limited performance within 20″ of stars as faint as $m_R = 12$ (R-band magnitude of 12) and attain partial correction on stars as faint as $m_R = 14$. The Keck NGS AO system and its performance is characterized in van Dam et al. (2004a). In spite of the success of NGS AO, the portion of the sky over which a sufficiently bright NGS exists is very limited. The laser guide star (LGS) AO system, on the other hand, can be used to observe any object within 60″ of tip-tilt (TT) reference stars as faint as $m_R = 19$, opening up about 70% of the sky to AO-corrected observation. Typical K-band Strehl ratios under normal seeing conditions vary from between 30% and 40% for bright reference stars to 10% for $m_R = 19$ reference stars.

The laser guide star adaptive optics system was developed for the Keck II Telescope to dramatically expand the region of the sky accessible to high spatial resolution imaging and spectroscopic observations. LGS AO systems have been implemented on other telescopes, with varying degrees of success (Lloyd-Hart et al. 1998; Fugate et al. 1994; Kasper et al. 2000; Davies et al. 2000). The Lick Observatory LGS AO system has been the most prolific such system from an astronomical point of view (Gavel et al. 2003).

First projection of the sodium-wavelength dye laser at Keck Observatory occurred in 2001 December, followed by the first LGS AO-corrected images in 2003 September (Wizinowich et al. 2004). Initial engineering science results can be found in Bouchez et al. (2004), while Wizinowich et al. (2006)

provides a detailed description of the system and its operation. We briefly review the components of the Keck LGS AO system here. The LGS AO system consists of all of the NGS AO components, with the addition of a sodium LGS, a sodium dichroic beam splitter, an NGS tip-tilt sensor (TTS), and an NGS low-bandwidth wave-front sensor (LBWFS). The corrected infrared beam can be directed to either the NIRC2 camera and spectrograph or the OSIRIS OH-suppressing integral field spectrograph.

The sodium dichroic beam splitter transmits light at 589 nm to the fast Shack-Hartmann wave-front sensor (WFS), while the remaining visible light is reflected to the avalanche photo-diode TTS (80%) and the LBWFS (20%). The TTS and the LBWFS ride on a three-axis positioning stage that allows them to acquire a tip-tilt reference star almost anywhere within a 60″ radius field from the optical axis.

In LGS AO operation, the TTS guides on the reference star using the TT mirror. Estimates of the higher order wave-front errors made by the WFS looking at the LGS are used to update the shape of the deformable mirror (DM). Any focus measured by the LBWFS is used to reposition the WFS focus stage and adjust the estimated altitude of the atmospheric sodium layer, thereby modifying the tracking rate of the WFS focus stage (Summers et al. 2004). Higher order aberrations in the reference star wave front measured with the LBWFS are used to modify the reference centroids on the WFS (i.e., the positions to which the WFS spots are driven). We call this process "image sharpening," since its effect is to eliminate any quasi-static error induced by the varying elongation of the LGS across the pupil of the telescope. Finally, the mean x- and y-centroids measured by the WFS are used to drive an uplink tip-tilt (UTT) mirror in the laser launch path, stabilizing the LGS on the WFS.

Wizinowich et al. (2006) contains a diagram summarizing the control loops.

Thus, during LGS AO observations, five feedback loops are operating simultaneously. The integration time and gain of each one must be optimized based on the atmospheric conditions and the magnitude and apparent size of the TT reference (TT, focus, and image-sharpening loops) and the LGS (DM and UTT loops). The UTT loop affects the wave-front error indirectly, since the position of the laser on the WFS is not used to drive any optic on the science image leg. However, since the positions of the spots on the WFS are measured with quad cells, a large mean deviation of the spots from the crosshairs of the quad cells causes a reduction in sensitivity of the WFS. The bandwidth and measurement errors from all the other loops contribute directly to the total wave-front error. In what follows, we describe the operation and performance of each subsystem, in addition to a method for calculating the associated wave-front error.

The aim of this paper is twofold. First, we quantify the performance of the system, since this is what matters to an astronomer who would be using it. Second, for each subsystem we describe the algorithms and the method of measuring the wave-front error. It is by minimizing the wave-front error in each subsystem that optimal image quality can be obtained. The wave-front reconstructor and the control loops of the subsystems are described in § 2. The performance of the system, described in § 3, is shown to be consistent with the error budget in § 4. Finally, conclusions are drawn in § 5.

2. SIGNAL PROCESSING

In this section, we describe the wave-front reconstructor and the control loops and characterize the performance of each susbsytem.

2.1. Wave-Front Reconstructor

The DM loop operates in the same way as it does for NGS AO: a Bayesian reconstructor inverts the poke matrix P using the covariances of Kolmogorov turbulence C_ϕ and of the relative noise in each subaperture W as prior information (van Dam et al. 2004b). There is a noise-to-signal parameter α that can be adjusted, depending on the brightness of the guide star and the strength of the seeing. The reconstructor R is given by

$$R = (P^T W^{-1} P + \alpha C_\phi^+ + \eta \mathbf{1} \mathbf{1}^T)^{-1} P^T W^{-1} G, \qquad (1)$$

where $\mathbf{1} = (1, 1, 1, \dots)^T$ and η is a piston penalization parameter needed to make the inversion well-conditioned. Its value is not critical and is set to 1. There are two differences between the NGS and the LGS reconstructors that stem from the elongation of the WFS spots in LGS AO with increasing subaperture distance from the launch telescope. First, the centroid gain is accomodated via a diagonal gain matrix, G. The relationship between the centroids and the displacement of the spot

is called the centroid gain. For a Shack-Hartmann WFS with quad cells, the centroid gain is inversely proportional to the spot size (Véran & Herriot 2000). Hence, the diagonal entries g_i are equal to the calculated WFS spot size on the sky, divided by the WFS spot size on the calibration light source. The centroids are thus premultiplied in the reconstruction process by the relative centroid gain. Consequently, the noise on each of the scaled centroids also differs, and this is accounted for in the weight matrix, W: each entry is proportional to g_i^2/I_i, where I_i is the intensity in subaperture i. The LGS reconstructor algorithm takes two inputs to estimate spot size in each subaperture and direction: the FWHM of the laser spot as seen from near the launch telescope and the maximum elongation observed from the far edge of the pupil. These parameters are a function of laser beam quality, seeing, and the thickness of the atmospheric sodium layer and are measured nightly from an acquisition camera image of the LGS taken with the segments of the primary mirror unstacked and the telescope pointed at zenith. Additional details of the implementation of the NGS reconstructor can be found in van Dam et al. (2004b).

2.2. Deformable Mirror Loop

The Shack-Hartmann WFS makes measurements of the wave front of the LGS and uses these to update the position of the DM. The controller is a Smith compensator with a variable gain and a leaky integrator (van Dam et al. 2004a). The frame rate of the WFS is varied between 200 and 660 Hz, depending on the seeing and the photon return from the LGS. The DM bandwidth and measurement noise errors are obtained from centroid diagnostics, which consist of 1000 consecutive frames of centroid data. The methodology used to extract the bandwidth and measurement noise wave-front errors from these data is described in detail in van Dam et al. (2004a). The centroid measurements are converted into wave-front space by multiplying by the reconstructor matrix to obtain the residual wave front. The power spectral density (PSD) of the residual wave front is plotted in Figure 1 for a WFS frame rate of 300 Hz. The measurement noise squared error is given by

$$\sigma_{\text{noise}}^2 = \sum \left| \frac{H(f)}{1 + H(f)} \right|^2 |N(f)|^2, \qquad (2)$$

where $H(f)$ is the open-loop transfer function of the AO system and the summation is over all the sampled discrete frequencies. The power spectrum of the noise, $N(f)$, is calculated from first principles using knowledge of the number of photons, dark current, and read noise. The determination of both $H(f)$ and $N(f)$ is described in detail in van Dam et al. (2004a). The residual wave front measured by the AO system consists of the uncorrected turbulence plus the measurement noise propagating through the control loop. The bandwidth error σ_{BW} is due to turbulence that is not compensated by the AO system. It is found by subtracting the noise from the measured residual
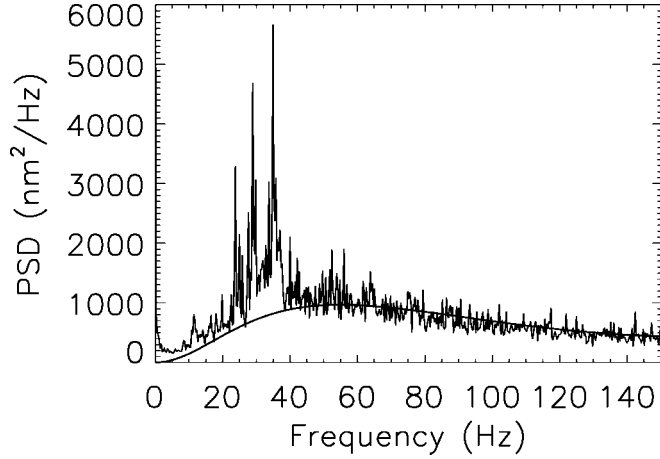
FIG. 1.—PSD of the residual wave front for the DM when guiding on the LGS. The theoretical noise PSD multiplied by the modulus squared of the rejection transfer function is superimposed.

wave-front power spectrum, $D(f)$:

$$\sigma_{\mathrm{BW}}^2 = \sum \left[|D(f)|^2 - \left| \frac{1}{1 + H(f)} \right|^2 |N(f)|^2 \right]. \qquad (3)$$

Figure 1 plots the PSD of the measured residual wave-front error, with the noise superimposed. This noise is subtracted to find the bandwidth error. From this set of residual wave fronts, we infer that the bandwidth and measurement noise errors are 157 and 142 nm, respectively.

2.3. Uplink Tip-Tilt Loop

The function of the UTT loop is to keep the LGS spots centered on the WFS. The UTT controller is an integral controller, with the mean x- and y-centroids of the illuminated subapertures on the WFS as its inputs. The rms deviation of the mean position of the spots from the center of the quad cells is between 50 and 120 mas in each direction. There are three reasons why the performance is substantially worse than that of the downlink tip-tilt loop. First, the uplink experiences much more turbulence than the downlink. Since the launch telescope is only 0.5 m in diameter, the rms value of the tip-tilt of the wave front over the aperture is substantially greater than for a 10 m aperture. In addition, the value of the tip-tilt decorrelates much more quickly over a 0.5 m aperture than over one 20 times the size. Second, the round-trip delay of the laser beam is at least 0.6 ms and increases with zenith angle, adding latency to the control loop. Third, due to the spot size elongation, the centroid gains are not the same; using the mean centroid as the tip-tilt estimate leads to a suboptimal estimate of the angle of arrival of the LGS. The decentering of the spot does not directly affect the image quality, since the downlink tip-tilt mirror guides on the tip-tilt star. However, there is a reduction

in the bandwidth of the DM loop, since the WFS does not always operate in the linear region of the quad cell.

2.4. Downlink Tip-Tilt Loop

The TTS consists of a quad cell of avalanche photodiodes. Its controller is a configurable four-tap infinite impulse response filter of the form

$$y(n) = -b_1 y(n-1) - b_2 y(n-2) - b_3 y(n-3) + a_0 u(n)$$
$$+ a_1 u(n-1) + a_2 u(n-2) + a_3 y(n-3), \qquad$$

$$(4)$$

where $u(n)$ and $y(n)$ are the inputs and outputs, respectively, at time n, and a_j and b_j are the filter coefficients. The transfer function of the controller can be written as

$$H_{\mathrm{TT}}(z) = \frac{a_0 + a_1 z^{-1} + a_2 z^{-2} + a_3 z^{-3}}{1 + b_1 z^{-1} + b_2 z^{-2} + b_3 z^{-3}}. \qquad (5)$$

Setting b_1 to -1, a_0 to k, and all the other coefficients to zero gives the standard integral controller, with a loop gain of k. The tip-tilt controller is also programmed to use an integrator that has a Bessel-Thomson low-pass filter with a configurable gain and frequency cutoff. For the case of faint stars, we find that the integral controller outperforms the Bessel-Thomson filter.

To find the true overall loop gain, it is also necessary to know the centroid gain, which depends on the size of the spot on the quad cells (Véran & Herriot 2000). The centroid gain can be calculated by closing both the DM and TT loops with the WFS while guiding on an NGS, moving the TTS stage by a known small amount, and measuring the change in the centroids with the TTS. While this method is accurate, it requires dedicated telescope time and so is not used during observations. Instead, the centroid gain is inferred visually by inspecting the noise component of the power spectrum and comparing it to the modeled rejection transfer function. The noise in the data is calculated in the following manner. The measured power spectrum, divided by the theoretical rejection transfer function, is averaged over the highest frequencies, where the amount of atmospheric turbulence in the power spectrum is negligible. The noise thus obtained agrees very well with the noise expected from a Monte Carlo simulation of the centroid error. The simple analytic formulae used to find the noise of the DM loop are not as accurate, since the variance of the denominator is significant when the tip-tilt star is faint. Figure 2 displays the PSD for magnitude 10.0 and 16.1 tip-tilt stars. The noise multiplied by the rejection transfer with the best-fit centroid gain is superimposed. The bandwidth and measurement noise errors are 109 and 23 nm for the 10.0 mag tip-tilt star and 161 and 129 nm for the 16.1 mag tip-tilt star.

It can be seen that the modeled noise matches the measured power spectrum. Interpreting the TTS residual power spectrum
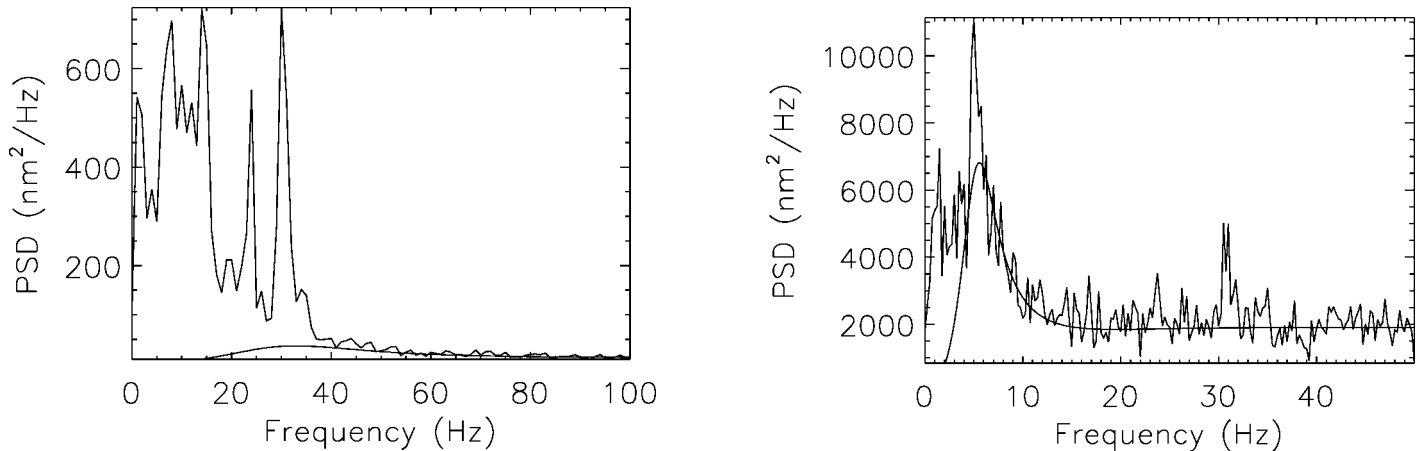
Fig. 2.—PSD of the residual wave front for the TTS when guiding on a star with an *R* magnitude of 10.0 (*left*) and 16.1 (*right*). The product of the noise PSD and the modulus squared of the rejection transfer function is superimposed.

is complicated because, for faint guide stars, the residual centroids are dominated by measurement noise. If the noise is not accurately modeled, it is very difficult to estimate the bandwidth error.

2.5. Image-sharpening and Focus Loops

The wave front sensed when guiding on the LGS differs from the residual wave front of the science target on the science camera. The focus for the LGS, which is located at an average height of about 90 km, differs from the focus of an object at infinity. Since the average height of the sodium layer changes with time, the focus of reference star must be tracked. There are also LGS aberrations, the origins of which are explained later in this section. As a result, a LBWFS guiding on an NGS is needed both to adjust the focus of the WFS stage and to sharpen the image by changing the reference centroids to eliminate the quasi-static higher order aberrations. Image sharpening is an iterative process and can been seen as an additional control loop. Its implementation is optimized to increase the sensitivity to faint starlight and minimize noise propagation. The WFS and LBWFS have the same number of subapertures and are registered to the DM in the same way; hence, they are also registered to each other. The reference centroids on the WFS and LBWFS are simultaneously calibrated with the shape on the DM that produces the best image on the science camera. Typical integration times on the LBWFS are 15 s on $m_R = 14$ stars and up to 120 s for $m_R = 19$ stars.

The steps involved in this focusing and image sharpening are as follows:

1. *Estimate LBWFS centroids.*—The LBWFS image is processed to subtract the dark current and is corrected for bad pixels. A maximum correlation method (Poyneer 2003) is used to locate and extract the spots in the frame and to compute the LBWFS centroids.

2. *Estimate the weight of each subaperture.*—The weight *w* for each subaperture is calculated from the magnitude of the maximum correlation between the observed spots and the reference spots. The weight map ranges from zero for unilluminated subapertures to unity for fully illuminated subapertures and is used to identify the extent of the illumination in each subaperture as the serrated hexagonal pupil of the telescope rotates.

3. *Estimate low-order terms ($\leq Z_{11}$).*—Estimates for the 10 lowest order Zernike coefficients a_2 to a_{11} are computed from the centroids using the expression for the Zernike derivative in Noll (1976). The tip-tilt terms are discarded, and the focus term is used to drive the focus stage. Zernike terms 5–11 are used to update the reference centroids in the fast WFS.

4. *Update the position of the WFS stage and the sodium height estimate.*—The position of the focus stage $Z_{LGS}(h, \zeta)$ is a function of the height of the sodium layer above the telescope, h, and the zenith angle ζ (Summers et al. 2004):

$$Z_{\mathrm{LGS}} = Z_{\mathrm{NGS}} + \frac{f^2 \cos \zeta}{h - f \cos \zeta}, \qquad (6)$$

where f is the focal length of the telescope. The focus term is converted into units of WFS stage motion ΔZ, and the WFS stage position at time n, $Z_{\mathrm{FCS}}(n)$, is updated in a integral feedback loop with variable gain g_F:

$$Z_{\mathrm{LGS}}(n) = Z_{\mathrm{LGS}}(n - 1) - g_F \Delta Z(n); \qquad (7)$$

the stage is then driven to its new position. Finally, the height of the sodium layer is updated every time the telescope is

moved to a new position:

$$h = \frac{f^2 \cos \zeta}{Z_{\mathrm{LGS}}(h, x) - Z_{\mathrm{NGS}}} - f \cos \zeta. \qquad (8)$$

This new value of h is used to update the position of the stage as ζ changes.

5. *Estimate high-order terms.*—The centroids corresponding to the measured Zernike terms are calculated and subtracted from the measured centroids to derive the higher order component for each illuminated subaperture:

$$\boldsymbol{c}_{\mathrm{HO}}(n) = \boldsymbol{c}(n) - \boldsymbol{c}_{\mathrm{LO}}(n), \qquad (9)$$

where LO and HO are used to denote the low- and high-order components of the LBWFS centroids $\boldsymbol{c}(n)$, which have units of arcseconds.

6. *Update WFS centroid references.*—There is an integral control loop with variable gain k and a leak factor l, typically set to 0.95 to prevent the accumulation of noise in the modes to which the LBWFS or the fast WFS are not very sensitive. The fast WFS reference centroids at time n, $\boldsymbol{r}(n)$, are updated from the measured LBWFS centroids according to

$$\boldsymbol{r}(n) = \boldsymbol{r}_{\mathrm{LO}}(n-1) - k\boldsymbol{g}^{-1}\boldsymbol{c}_{\mathrm{LO}}(n)$$
$$+ [1 - \boldsymbol{w}(1-l)]\boldsymbol{r}_{\mathrm{HO}}(n-1) - k\boldsymbol{g}^{-1}\boldsymbol{w}\boldsymbol{c}_{\mathrm{HO}}(n), \quad (10)$$

where $\boldsymbol{w}$ is the vector of subaperture weights calculated in step 2. The absolute centroid gain of the fast WFS quad cells, $\boldsymbol{g}$, converts WFS centroid units into arcseconds of displacement and differs for each axis of every subaperture. For stars with $m_R > 17$, only the low-order reference centroids are updated:

$$\boldsymbol{r}(n) = \boldsymbol{r}_{\mathrm{LO}}(n-1) - k\boldsymbol{g}^{-1}\boldsymbol{c}_{\mathrm{LO}}(n). \qquad (11)$$

Figure 3 illustrates the improvement in performance provided by image sharpening. In this case, the Strehl ratio increased from 8% to 33%. In position angle mode, where the field stays fixed on the science camera at a Nasmyth focus, the pupil and LGS elongation pattern rotate on the WFS and LBWFS, and the WFS reference centroids must be updated accordingly. This causes difficulties when observing with TT reference stars fainter than 17 mag, as the required WFS centroid corrections may change more rapidly than they can be estimated using the LBWFS. We have developed an empirical model for these aberrations as a function of the pupil angle and elevation that can be used to update the fast WFS reference centroids without using the LBWFS. Unfortunately, these aberrations and the centroid gain of the WFS vary from night to night. There are a number of sources of quasi-static aberrations resulting from the use of an LGS. First, the increase in spot elongation with increasing distance from the LGS gives rise to aberrations that are symmetrical about the location of the
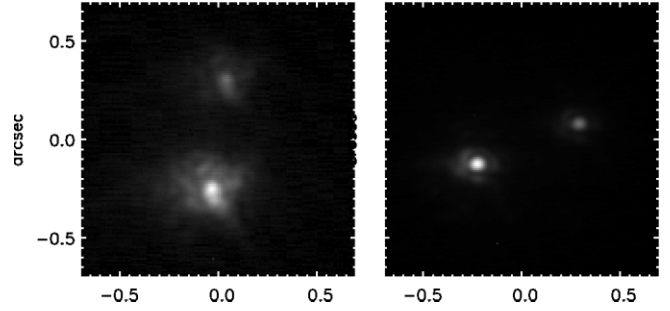

FIG. 3.—Images (20 s) at 2.15 μm of the 0″.56 binary star TYC 1467-935-1. The DM was closed on the LGS and the TT loop on the $V = 10.0$ binary. *Left*: Image taken after offloading the focus measured with the LBWFS to the DM focus stage (step 4), but before image sharpening (steps 5 and 6). The Strehl ratio is 8%. *Right*: Image following image sharpening, at a different position angle. The Strehl ratio is 33%.

launch telescope. This is especially severe for the Keck LGS AO system, since the laser is side projected. This effect is highly asymmetric, since not only is the distribution of the sodium asymmetric, but the spot elongation itself is asymmetric. The elongation is inversely proportional to height, so the elongation due to sodium at 80 km is more severe than the elongation due to sodium at 100 km. This difference in elongation introduces a bias in each centroid measurement in the direction of the LGS. To further compound the situation, the quad cell centroid does not coincide with the center of mass if the spot is asymmetric. Furthermore, the bias in the centroids depends on the direction of the elongation relative to the alignment of the quad cell. Other sources of bias include the truncation of the spot due to the finite extent of the quad cells (2″.1 × 2″.1 pixels) and the finite extent of the circular field stop, which has a diameter of 4″.8. There are other optical aberrations introduced by the telescope or AO system that are related to the difference in focus between the LGS and the NGS.

Figure 4 shows a representative example of the first four Zernike coefficients that are compensated using the reference centroids in the WFS. The magnitude of the LGS aberrations, which are shown for a zenith angle of 20°, decrease with increasing zenith angle. The aberrations are plotted as a function of pupil angle, which represents the location of the laser relative to the wave-front sensor. The laser launch telescope is located at the top of the pupil, at a pupil angle of 116°.6.

3. PERFORMANCE OF THE LGS AO SYSTEM

In this section, we document the measured performance of the Keck LGS AO system and show that the image quality is consistent with what is expected from the performance of the subsystems and the atmospheric conditions. For a given set of atmospheric conditions, the point-spread function (PSF) of the science image depends on four external factors: the visual magnitude of the tip-tilt guide star, the elevation, the distance be-
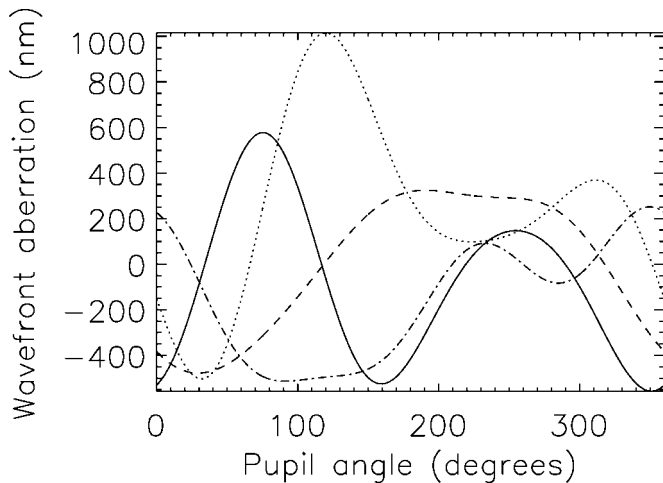
Fig. 4.—Measured LGS aberrations as a function of pupil angle. The curves represent 45° astigmatism (*solid line*), 0° astigmatism (*dotted line*), *y*-coma (*dot-dashed line*) and *x*-coma (*dashed line*).

tween the NGS and the science object (angular anisokinetism), and the distance between the LGS and the science object (angular anisoplanatism). In LGS AO, angular anisoplanatism and anisokinetism can be treated separately.

It is important to note that all the individual performance characterization tests reported here were performed on different nights with differing observing conditions and an evolving LGS AO system. The results are presented to give a flavor of what the typical performance is and how we measure and understand the performance attained. The Keck LGS AO Web page[1] contains updated information on the performance and limitations of the system.

The Strehl ratio is the most commonly used metric for image quality. It is defined as the peak intensity of the image divided by the peak intensity of the diffraction-limited PSF. The Strehl ratio decreases monotonically with increasing wave-front error, and for this reason it is popular as a measure of image quality in AO. The algorithm used to measure the Strehl ratio from science images is Method Seven, reported in Roberts et al. (2004). In addition, we also measure the FWHM of the PSF, since this determines the resolution of the AO system.

Frequently, error budgets are computed by assuming that all the error terms add independently. This assumption is not strictly correct, since there is an interaction between the different error terms. For example, both the limited bandwidth of the TT controller and a large angle between the TT guide star and the science target result in an inability to measure high temporal frequency tip-tilt aberrations. Hence, care must be taken to avoid double-counting the errors. However, for the AO system, with both the NGS tip-tilt star and the laser on-axis, the approximation of statistical independence is valid. In

this section, we first present an error budget for the LGS AO system using a bright guide star. Since the corresponding measured Strehl ratios S are sufficiently high, the Maréchal approximation

$$S = \exp\left[-(2\pi\sigma_W/\lambda)^2\right] \quad (12)$$

can be invoked to show that the rms wave-front error σ_W is consistent with the image quality at imaging wavelength λ. For the case of faint guide stars, the tip-tilt error is large and equation (12) no longer holds, so the PSF from a bright guide star is convolved with the residual image motion to calculate the Strehl ratio.

3.1. Strehl Ratio versus Tip-Tilt Star Magnitude

Figure 5 displays the measured Strehl ratios and FWHM values as a function of tip-tilt guide star magnitude. The performance degrades due to the reduced bandwidth of the tip-tilt correction and the increased errors in measuring focus and higher order aberrations. The night-to-night performance difference is due to the difference in atmospheric conditions. The curves in Figure 5 are representative of the performance to be expected in all but the worst 25% of the nights. The performance of an LGS AO system cannot be simply characterized by the seeing and the atmospheric decorrelation: the Strehl ratio also depends on the height of the turbulence, the sodium density and structure, and the tip-tilt power spectrum.

3.2. Strehl Ratio versus Zenith Angle

The Strehl ratio was measured as a function of zenith angle using a bright tip-tilt guide star on three different nights in 2005. The results displayed in Figure 6 show a remarkable degradation in performance with air mass.

The image quality degrades much more with increasing air mass than for the NGS, because there are many terms in the LGS error budget that are not in the NGS AO error budget that also increase in magnitude with increasing air mass. The focal anisoplanatic error of equation (16) is proportional to air mass. The photon return of the LGS decreases at a faster rate than the square of the distance to the beacon, since more scattering occurs at higher air masses. In addition, the error in measuring tip-tilt is inversely proportional to the spot size on the tip-tilt sensor, which also increases with increasing air mass. At a high air mass, however, the focus will drift less and the spot elongation is also reduced, resulting in smaller focus and other quasi-static errors.

3.3. Angular Anisoplanatism

Because the tip-tilt decorrelation does not contribute to LGS angular anisoplanatism, the isoplanatic angle in LGS AO is larger than for NGS AO. In addition, because an LGS samples a cone of turbulence rather than the cylinder that the NGS samples, the sampled turbulence decorrelates more slowly with
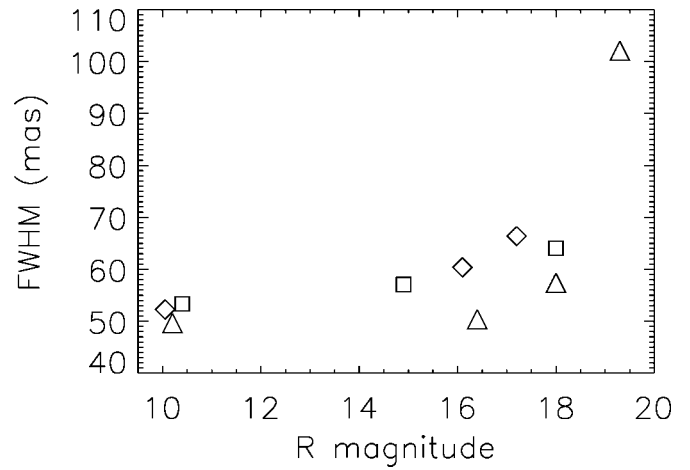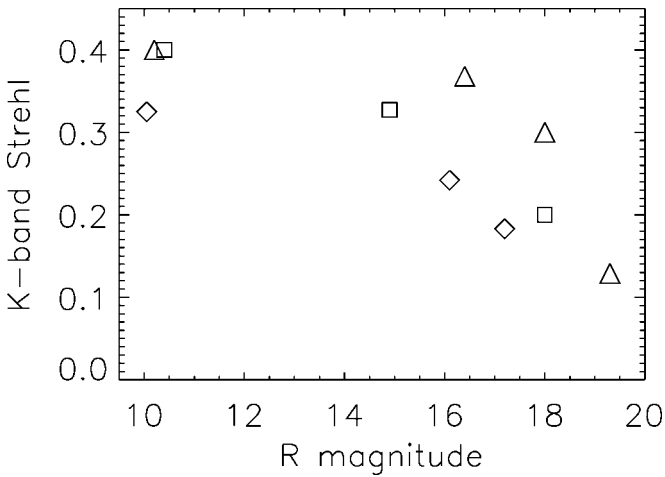
FIG. 5.—Strehl (*left*) and FWHM (*right*) vs. tip-tilt guide star magnitude. Squares, diamonds, and triangles represent data from three different nights in 2005.

isoplanatic angle. Another way to see this is that the isoplanatic error depends on the highest spatial frequency that is measured and corrected (Molodij & Rousset 1997), and the highest corrected spatial frequency is reduced due to focal anisoplanatism.

Figure 7 displays the results from the measurement of the isoplanatic angle. Here images of the tip-tilt star were captured with the LGS at different separations from the star. Using the expression for NGS AO isoplanatic angle θ_0 given by equation (9.24) in Hardy (1998),

$$\sigma_{AA}^2 = (\theta/\theta_0)^{5/3}, \qquad (13)$$

we find the best-fit line to be for an isoplanatic angle of $45''$ in the K band. On a subsequent night, the isoplanatic angle was measured to be $35''$.

3.4. Angular Anisokinetism

The anisokinetic error is due to the error in estimating the tip-tilt, which is the result of the decorrelation between the tip-tilt at the science object and at the tip-tilt guide star. The error is

$$\sigma_{TA}^2 = (\theta/\theta_{TA})^2 \qquad (14)$$

in terms of the isokinetic angle, θ_{TA}. For angles less than about $D/40,000 = 51''6$, θ_{TA} is given by equation (7.62) in Hardy (1998):

$$\theta_{TA} = \left[0.668 D^{-1/3} (\sec \zeta)^3 \int_0^H C_N^2(z) z^2 \, dz\right]^{-1/2}. \qquad (15)$$
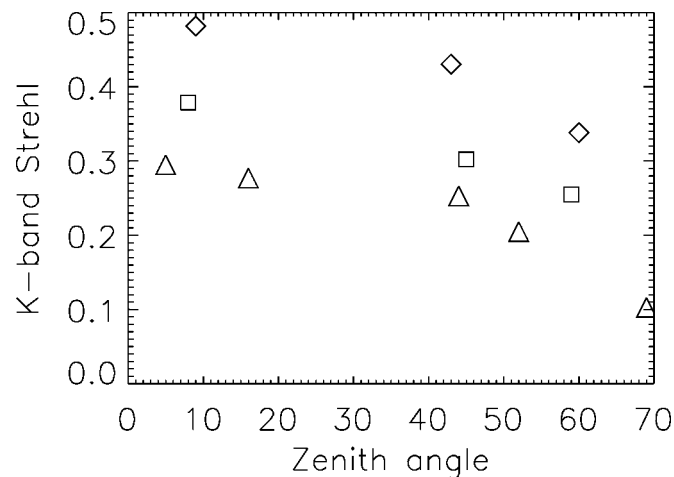

FIG. 6.—Strehl vs. zenith angle for a bright tip-tilt guide star. Squares, diamonds, and triangles represent data from three different nights in 2005.
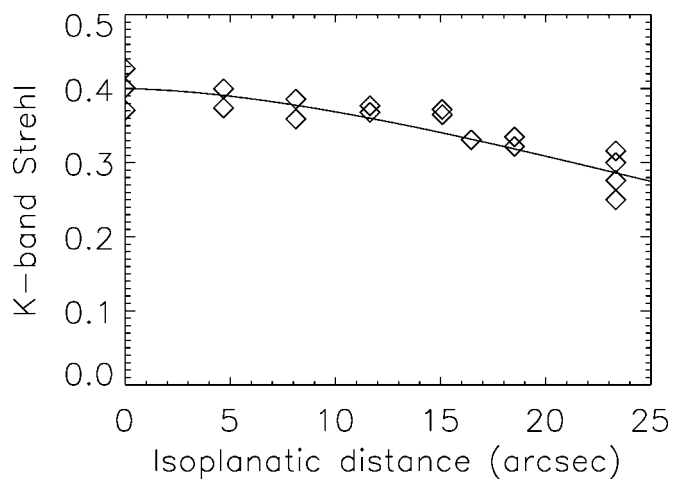

FIG. 7.—Strehl vs. angular separation from the LGS.

The turbulence profiles in Tokovinin et al. (2004) give rise to estimates between 37″ and 51″ for the *K*-band isokinetic angle.

We made measurements of the isokinetic angle by measuring the Strehl ratio at a bright tip-tilt star and then at a star offset from the tip-tilt star by 20″–40″. In both cases, the laser was centered on the star being imaged. The Strehl degradation was used to calculate the isokinetic angle via equation (14) and was corrected for the air mass by dividing by $(\sec \zeta)^{3/2}$. The average isokinetic angle at zenith was found to be 64″, 73″, and 95″ on three different nights.

4. ERROR BUDGET

4.1. Bright Tip-Tilt Star Error Budget

The error budget for a bright TT guide star, typically with $m_R = 10$, is presented in Table 1. The total wave-front error, obtained from science images via the Maréchal approximation, agrees with the wave-front error from the error budget. In fact, the Maréchal approximation underestimates the wave-front error, so there are additional errors that have not been accounted for. Nevertheless, it is clear that a good understanding of the magnitude of the dominant error terms has been achieved. The bright guide star Strehl ratio could be increased by reducing the DM measurement noise and bandwidth errors. This can be accomplished by reducing the read noise and charge diffusion of the CCD and reducing the latency of the wave-front controller. We are in the process of upgrading the wave-front sensor and the wave-front controller to obtain these benefits. In addition, having a more powerful laser and projecting it from behind the secondary mirror would also reduce the DM error terms: both of these changes will be implemented with the planned LGS upgrade to the Keck I AO system.

The atmospheric and telescope fitting errors are the same as for NGS AO and are obtained from van Dam et al. (2004a). The camera error is also the same as for NGS AO, but the method for calibrating the non–common-path errors of the AO system is improved from that reported in van Dam et al. (2004a). A modified Gerchberg-Saxton phase-diversity algorithm similar to that reported in Atcheson et al. (2003) is used to obtain the shape on the DM that gives the best image quality on an actuator-by-actuator basis.

The wave-front error due to focal anisoplanatism is given by equation (7.35) in Hardy (1998), and assuming that there is no turbulence above the laser beacon, it can be restated as

$$\sigma_{FA}^2 = D^{5/3} \left[0.500 H^{-5/3} (\sec \zeta)^{8/3} \int_0^H C_N^2(z) z^{5/3} \, dz \right.$$

$$\left. - 0.452 H^{-2} (\sec \zeta)^3 \int_0^H C_N^2(z) z^2 \, dz \right], \quad (16)$$

where D is the diameter of the telescope, H is the height of the sodium layer, and $C_N^2(z)$ is the turbulence structure function

TABLE 1
Bright Star LGS AO Error Budget

Source	σ_W
Atmospheric fitting	128
Telescope fitting	60
Camera	50
DM bandwidth	157
DM measurement	142
TT bandwidth	109
TT measurement	23
LGS focus error	36
LGS high-order error	80
Focal anisoplanatism	175
Total wave-front error	357
Predicted Strehl (2.12 μm)	35%
Measured Strehl (2.12 μm)	35%

NOTE.—The rms wave-front errors σ_W are quoted in nanometers.

at height z above the telescope. The focal anisoplanatism value was calculated theoretically from Mauna Kea C_N^2 profiles measured using SCIDAR (scintillation detection and ranging) and reported in Tokovinin et al. (2004). The average turbulence profile over each of the four nights was inserted into equation (16) to obtain wave-front error estimates ranging between 143 and 192 nm, with a mean value of 175 nm. The effect of focal anisoplanatism depends on the highest spatial frequency corrected. Spatial frequencies higher than those measured by the WFS and corrected by the DM also decorrelate due to focal anisoplanatism, but this decorrelation is inconsequential. Hence, equation (16) overestimates the magnitude of the wave-front error (Molodij & Rousset 1997).

4.2. Tip-Tilt Degradation with Guide Star Magnitude

As the guide star becomes fainter, the Strehl ratio is reduced and the relationship between the wave-front error and the Strehl ratio no longer obeys the Maréchal approximation. In order to determine what Strehl ratio should be expected as a function of wave-front error, the following calculation was performed. The PSF obtained on a bright guide star was convolved with a Gaussian PSF, the width of which corresponds to the rms tip-tilt wave front. An image motion of 1″ corresponds to 12.68 μm of wave-front error for the Keck Telescope pupil. In these measurements, the image sharpening and focus had just been performed on a bright, nearby tip-tilt guide star, so the increase in error is solely due to an increase in the tip-tilt error. Table 2 tabulates the wave-front error as a function of tip-tilt star brightness.

Figure 8 displays the measured and predicted Strehl ratios and FWHM as a function of tip-tilt guide star magnitude. The FWHM estimates from tip-tilt residuals agree very well with the measured values.

5. CONCLUSION

The Keck LGS AO system has been characterized. The performance attained, with Strehl ratios of 0.35 for bright tip-tilt
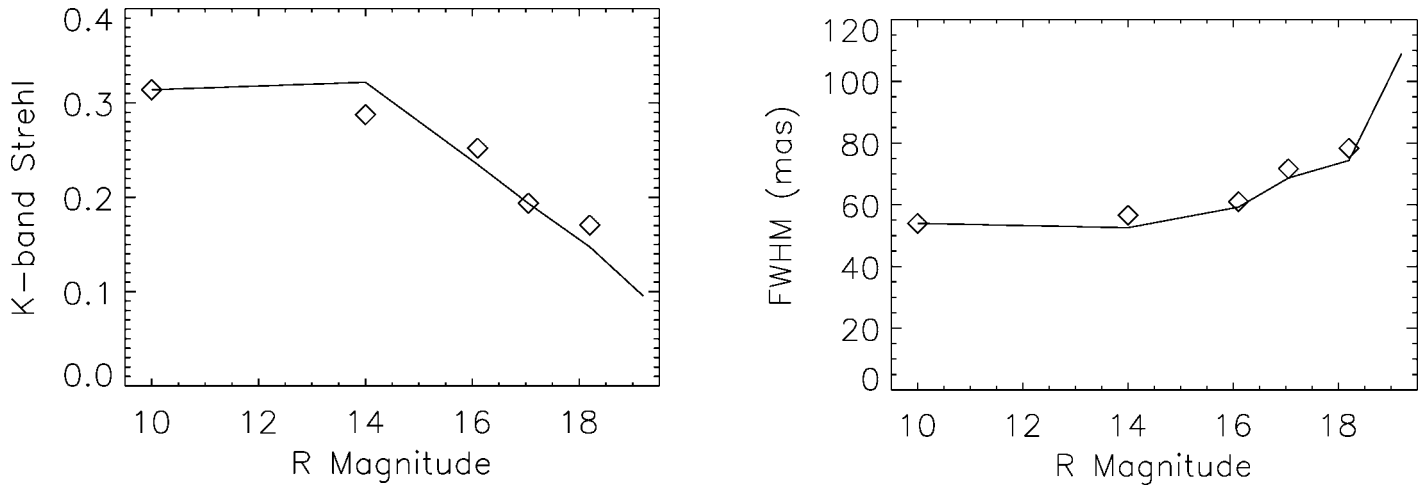
F𝗂𝗀. 8.—Strehl (*left*) and FWHM (*right*) vs. tip-tilt guide star magnitude. The solid line is a fit to the measurements from the images, and the diamonds represent estimates from the tip-tilt residuals.

stars, is consistent with the error budget. As the magnitude of the tip-tilt star increases, the degradation in image quality is also consistent with telescope data. The LGS AO system is useful for tip-tilt guide stars as faint as 19 mag. Understanding the behavior of the LGS quasi-static aberrations has proved to be the biggest difficulty in characterizing the system. Further testing on the Keck Telescope, and the experience gained on other 5–10 m class telescopes, will be useful in improving the understanding of these aberrations.

TABLE 2
T𝗂𝗉-T𝗂𝗅𝗍 𝗋𝗆𝗌 W𝖺𝗏𝖾-F𝗋𝗈𝗇𝗍 R𝖾𝗌𝗂𝖽𝗎𝖺𝗅 E𝗋𝗋𝗈𝗋
𝖺𝗌 𝖺 F𝗎𝗇𝖼𝗍𝗂𝗈𝗇 𝗈𝖿 G𝗎𝗂𝖽𝖾 S𝗍𝖺𝗋 M𝖺𝗀𝗇𝗂𝗍𝗎𝖽𝖾

rms Error (nm)	*R* Magnitude
111	10.0
164	14.0
230	16.1
342	17.1
397	18.2

REFERENCES

Atcheson, P. D., Acton, D. S., & Lightsey, P. A. 2003, Proc. SPIE, 4839, 228
Bouchez, A. H., et al. 2004, Proc. SPIE, 5490, 321
Davies, R., Eckart, A., Hackenberg, W., Ott, T., Butler, D., Kasper, M., & Quirrenbach, A. 2000, Exp. Astron., 10, 103
Fugate, R. Q., et al. 1994, J. Opt. Soc. Am. A, 11, 310
Gavel, D. T., et al. 2003, Proc SPIE, 4839, 354
Hardy, J. W. 1998, Adaptive Optics for Astronomical Telescopes (New York: Oxford Univ. Press)
Kasper, M., Looze, D. P., Hippler, S., Herbst, T., Glindemann, A., Ott, T., & Wirth, A. 2000, Exp. Astron., 10, 49
Lloyd-Hart, M., et al. 1998, ApJ, 493, 950
Molodij, G., & Rousset, G 1997, J. Opt. Soc. Am. A, 14, 1949

Noll, R. J. 1976, J. Opt. Soc. Am., 66, 207
Poyneer, L. A. 2003, Appl. Opt., 42, 5807
Roberts, L. C., et al. 2004, Proc. SPIE, 5490, 504
Summers, D., et al. 2004, Proc. SPIE, 5490, 1117
Tokovinin, A., Vernin, J., Ziad, A., & Chun, M. 2004, PASP, 117, 395
van Dam, M. A., Le Mignant, D., & Macintosh, B. A. 2004a, Appl. Opt., 43, 5458
———. 2004b, Proc. SPIE, 5490, 174
Véran, J.-P., & Herriot, G. 2000, J. Opt. Soc. Am. A, 17, 1430
Wizinowich, P. L., et al. 2004, Proc. SPIE, 5490, 1
———. 2006, PASP, 118, 297